CrossMark

Thermal and physical properties of ZrO$_2$–AlO(OH) nanopowders synthesised by microwave hydrothermal method

Iwona Koltsov[1] · Marta Prześniak-Welenc[2] · Jacek Wojnarowicz[1] · Anna Rogowska[1] · Jan Mizeracki[1] · Maria Malysa[1] · Giora Kimmel[3]

Abstract Industrially relevant nanopowder was synthesised by microwave hydrothermal synthesis to obtain well-controlled composition (ZrO$_2$–AlO(OH) system) which was found to determine a number of physical and thermal characteristics. This study reports variation of particle size, density, specific surface area (SSA$_{BET}$), as well as thermal behaviour of nanopowder mixtures of ZrO$_2$–AlO(OH) in the whole range of compositions. It was found that the onset temperature (T_{on}) of physically and chemically bounded water desorption depends on the Al^{3+}/or AlO(OH) content. The lower content of Al^{3+} in the ZrO$_2$–AlO(OH) system, the higher T_{on} of physically bound water desorption. There are three distinct temperature regions for water decomposition for nanomaterials investigated in air (at approximately 50, 250 and 450 °C). These temperature ranges depend on particle size and chemical composition of ZrO$_2$–AlO(OH) nanopowders. Materials were divided into three groups characterised by different properties: (1) ZrO$_2$ with 2–12% of Al^{3+}, where particle sizes are from 4 to 8 nm, (2) ZrO$_2$ with 30–67% of AlO(OH), where particle sizes are from 10 to 13 nm, and (3) ZrO$_2$ with 80–99% of AlO(OH), where particle sizes are from 13 to 23 nm. AlO(OH) content determines thermal and physico-chemical properties of synthesised ZrO$_2$–AlO(OH) nanopowders.

Introduction

It is well known that nanoparticle size, shape, surface chemistry, dispersibility or sinterability are dependent on external factors such as temperature, humidity or level of contamination as well as being time dependent. This has implications for industry, standardisation community and regulators. Fundamental questions of sell-by date for nanomaterial, environmental fate, toxicology and usability in applications are being asked. It is known that nanomaterials have a large specific surface area and that their properties are often governed by surface processes. The dynamics of such processes (agglomeration, dispersion or sintering) are determined by external factors as well as internal energy transitions. This presents a complex problem where chemistry of material as well as its surface, particle size and shape affect dynamics and practical applications. One of such commercial applications is the use of sintered ZrO$_2$-based ceramics which are industrially relevant nanomaterials in medical implants and dentistry. Amongst other factors, thermal behaviour of nanopowders is one of the most influential factor in this material system governing material parameters. Chemical bonding of –OH groups and physisorption of H$_2$O on the surface depend on material composition and its particle size. Their presence may influence densification and sintering processes [1].

Nanomaterials used in biomedical applications, especially the ones in implant and prosthetics applications area received a lot of attention in recent years [2]. One of the

✉ Iwona Koltsov
iwona@unipress.waw.pl

1 Institute of High Pressure Physics, Polish Academy of Sciences, Sokolowska 29/37, 01-142 Warsaw, Poland

2 Faculty of Applied Physics and Mathematics, Gdansk University of Technology, Narutowicza 11/12, 80-233 Gdańsk, Poland

3 Ben-Gurion University of the Negev, 8410501 Beersheba, Israel

most promising bio-compatible materials systems is a ceramic based on ZrO_2. Synthesis of such ceramics presents a number of challenges [3]. For a good sinterability, synthesis of ZrO_2-based ceramic powders with narrow particle size distribution is of considerable interest [4]. Relative to their conventional micron-sized crystalline counterparts, nano-ZrO_2-based ceramics demonstrate better materials properties and superplastic behaviour [5–8]. Therefore, nanograined ceramics hold promise of unique mechanical properties that are not commonly found in coarse-grained counterparts [9].

Generally, ZrO_2 in the equilibrium state exists in three polymorphic forms: monoclinic (m-ZrO_2), tetragonal (t-ZrO_2) and cubic (c-ZrO_2) [10]. The amount and type of dopant and the synthesis route may determine the phases of the crystalline product [11]. From existing crystallographic forms of ZrO_2, the tetragonal phase is the most demanded phase because of its mechanical properties. From crystallographic X-ray studies, it is not possible to distinguish t-ZrO_2 and c-ZrO_2 phases [4] due to the overlap of their characteristic diffraction lines.

The required t-ZrO_2 phase is very often stabilised by additional compounds such as yttria (Y_2O_3) [4]. However, it was found that t-ZrO_2 can be stabilised at room temperature by doping divalent or trivalent cations such as Ca^{2+} or Al^{3+} which are much less expensive than Yttrium ions [12, 13]. The XRD studies show that the structure remains unaltered even after 10 mol% of Al^{3+} doping, confirming the stability of such crystalline structure [12]. This opens a perspective for cost-effective synthesis and sintering of bulk materials made from zirconia–alumina alloys. Zirconia–alumina nanomaterials amongst other advanced ceramics show superior mechanical properties, chemical inertness and biocompatibility. They are used for a wide range of applications such as biomedical implants [14, 15] and structural ceramics [16, 17].

The production process of ZrO_2–Al_2O_3 (ZrO_2–AlO(OH)) nanopowders follows various chemical routes, such as sol–gel method [4, 18–20], hydrothermal synthesis [21, 22] or co-precipitation method [23, 24]. It was found [25] that the main benefit of hydrothermal synthesis is the generation of weakly agglomerated nanopowder. However, some research suggests difficulties in reproducing and controlling properties of these nanopowders [25, 26]. That is because the synthesis of ZrO_2–Al_2O_3 ceramics is highly sensitive to synthesis parameters, including concentration, temperature, pH and drying method [9]. Also, synthesis conditions influence density, specific surface area, phase composition of ZrO_2–Al_2O_3 [26, 27] and the amount of adsorbed water.

On the other hand, sintering properties of nanomaterials depend on the green body micro- and nanostructure [28]. It is also required that the pores are in the nanometre size range, since large pores may grow during synthesis [28]. The green body nanostructure depends strongly on the viscosity of the slurry used for its production, which in turn depends on the amount of water physically or chemically bounded to the nanoparticles. Cinar et al. [27] showed that nanopowder suspensions based on ZrO_2–Al_2O_3 are characterised by higher viscosities compared to micron size powders. The lower viscosity indicates poor dispersion of nanopowder with a lot of aggregates. Higher viscosity indicates that all particles are contributing to the dynamics of the liquid due to the increased solid–liquid contact around particles [27]. Cinar et al. [27] also showed that high viscosity of powders is linked to the bound water on particle surface. It was explained that bound water, which exists around the nanoparticles, does not function as a solvent in the system, but behaves as a part of the powder. This fact leads to the change of viscosity. Thus, for optimal green body formation technology, it is required to control existence and amount of bound water around the nanoparticles.

This work evaluates the impact of composition (in ZrO_2–AlO(OH)) on physical and thermal parameters such as water decomposition, onset temperature of ZrO_2–AlO(OH) phase transformations, as well as zeta potential, density, particle size, and SSA_{BET}.

The novelty of this paper is the discussion of characterisation results and thermal behaviour of ZrO_2–AlO(OH) nanopowders (synthesised by MHS method) with different amounts of AlO(OH) in a whole range of compositions (from 2 to 99% of Al^{3+}). Pure ZrO_2 and χ-AlO(OH) were used as a references. The boehmite (χ-AlO(OH)) phase transforms into Al_2O_3 after annealing which we already reported [29]. However, in this work we describe results
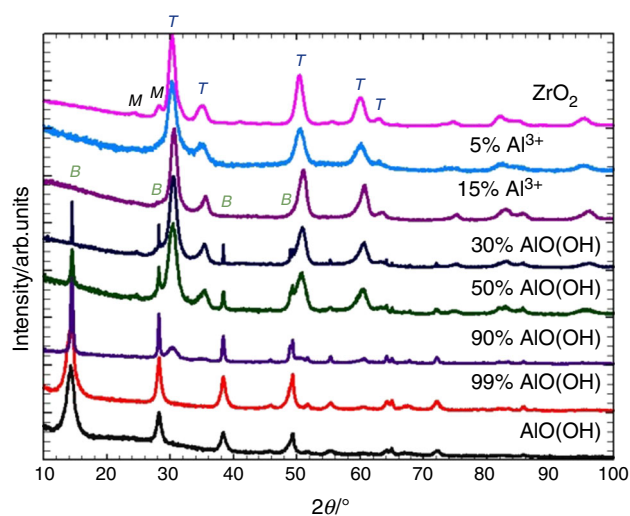
Fig. 1 XRD patterns for as-synthesised ZrO_2, AlO(OH) and ZrO_2 with chosen Al^{3+} or AlO(OH) additive, where M, T and B represent m-ZrO_2, t-ZrO_2 and Boehmite phases, respectively

Fig. 2 SEM images for chosen ZrO_2–AlO(OH) nanopowders, where **a** is ZrO_2, and ZrO_2 with **b** 5% Al^{3+}, **c** 12% Al^{3+}, **d** 50% AlO(OH), **e** 90% AlO(OH) and **f** AlO(OH)
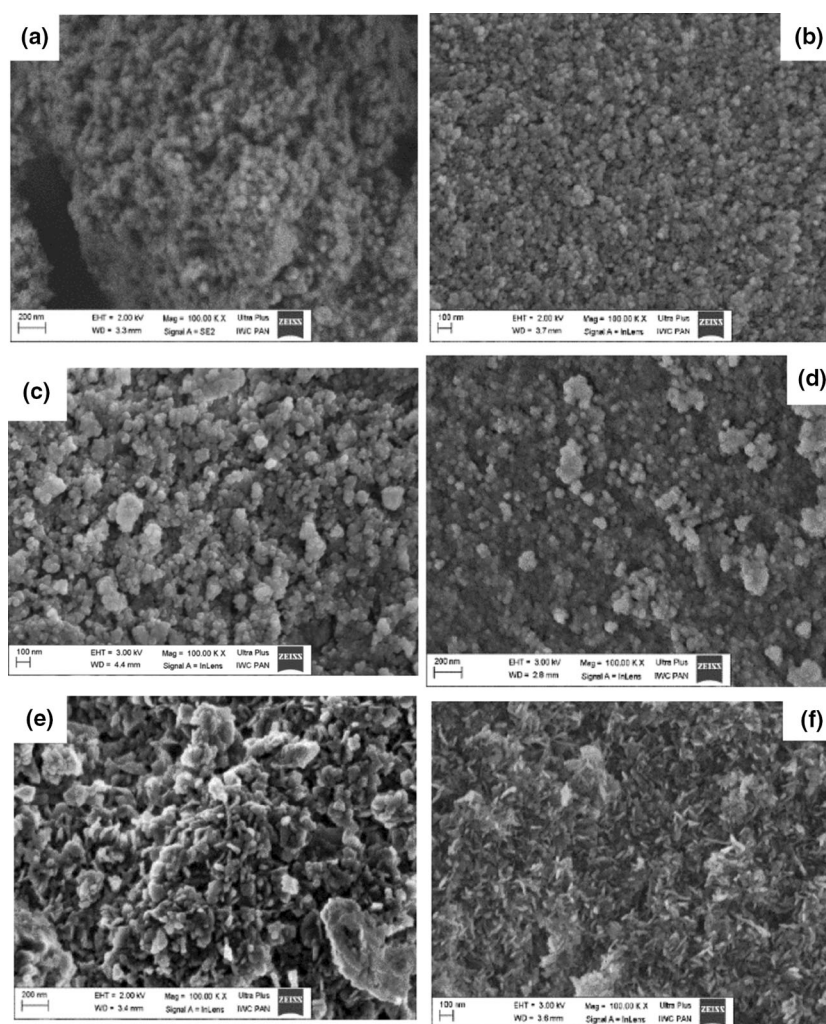
obtained only for as-synthesised powders in order to preserve water content and analyse it in detail. Applied synthesis method allows to create fully crystalline product in contrary to the traditional sol–gel synthesis. Our results demonstrate the complexity of processes taking place in nanomaterials. This work may be helpful to track nanomaterials ageing process and material selection for various applications.

Nanopowders synthesis and characterisation methods

Various compositions of ZrO_2–χ-AlO(OH) nanopowders were synthesised using microwave- hydrothermal synthesis. The reagents used in the process were: zirconyl chloride octahydrate [$ZrOCl_2\cdot 8H_2O$ Sigma-Aldrich ($\geq$ 99.5%)], sodium hydroxide (CHEMPUR, analytically pure) and aluminium nitrate non-ahydrate [$Al(NO_3)_3\cdot 9H_2O$ CHEMPUR, analytically pure]. The reagents were used

without additional purification. Deionised water with specific conductance below 0.1 μS cm^{-1} was obtained using a deioniser (HLP 20UV, Hydrolab, Poland). Microwave reactions took part in a MAGNUM II ERTEC microwave reactor (2.45 GHz, 600 W). The reaction parameters were set as follows: $T = 258$–263 °C, $P = 50$–56 atm, heating time = 20 min. The details of the hydrothermal synthesis method were reported previously [29]. Calculations for all compositions were done for mass% of AlO(OH) needed to obtain such amount of Al_2O_3 (in ZrO_2–Al_2O_3) after annealing.

Scanning electron microscopy (SEM) analysis for ZrO_2–AlO(OH) nanopowders was performed on carbon-coated samples using Zeiss Ultra Plus scanning electron microscope.

The low-temperature differential scanning calorimetry and thermogravimetry (LT-TG–DSC) experiments were carried out on a STA 449 F1 *Jupiter* by Netzsch using stainless steel furnace. The experiments were performed with a heating rate of 10 °C min^{-1} from − 150 °C up to
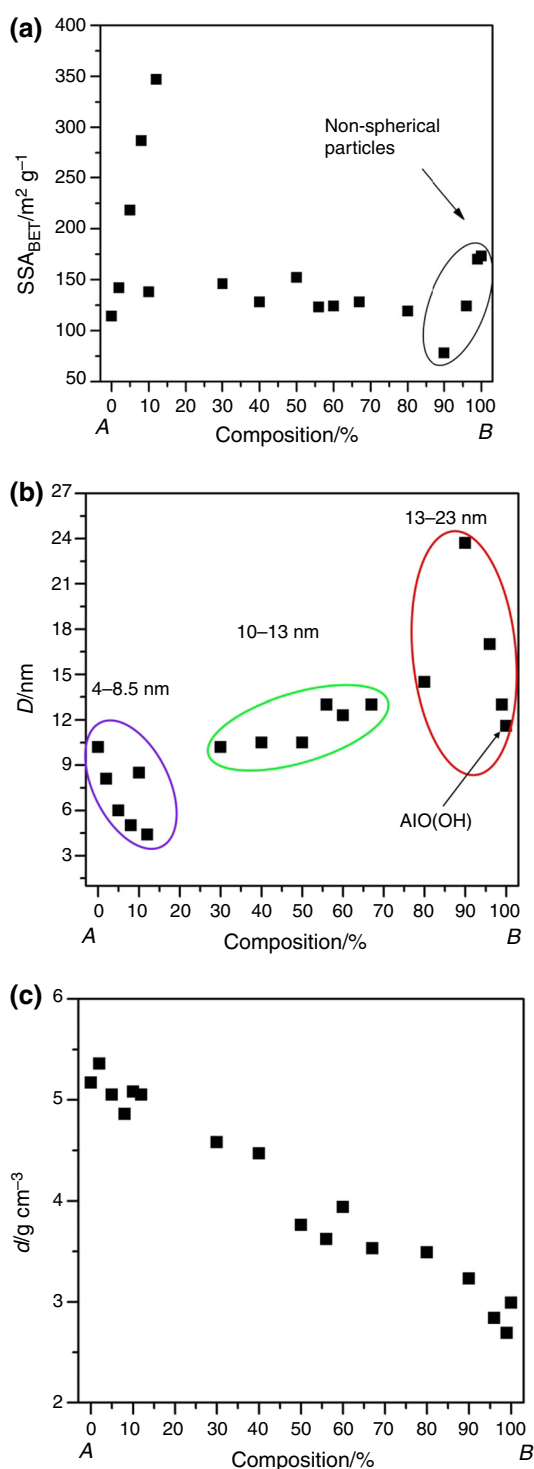
Fig. 3 Dependence of SSA$_{BET}$ values, particle size (D) obtained from SSA$_{BET}$, and density (d) for ZrO$_2$ on different AlO(OH) content, where $A = 100\%$ ZrO$_2$ phase, $B = 100\%$ AlO(OH) phase. **a** SSA$_{BET}$ as a function of composition, **b** D as a function of composition and **c** d as a function of composition

800 °C. Constant flow of helium at 60 mL min^{-1} was applied. For each experiment, we used approximately 30 mg fine (previously mortared) powder which was

pressed into crucible prior each measurement. In order to obtain reproducible results, samples were outgassed without heating before the start of each experiment.

The high-temperature differential scanning calorimetry and mass spectrometry (HT-DSC–MS) analyses were performed using a STA 449 F1 *Jupiter* by Netzsch equipped with SiC furnace. The experiments were carried out with a heating rate of 10 °C min^{-1} from ambient temperature up to 1450 °C, where a constant flow of air (60 mL min^{-1}) was applied. The volatile products emitted during heating were detected with a mass spectrometer (QMS 403C Aeolos) coupled in line with the STA instrument.

X-ray diffraction patterns of nanopowders were obtained on X'Pert PRO, PANalytical diffractometer equipped with a copper anode (CuKα_1) and an ultra-fast PIXcel[1D] detector. The analysis was performed at room temperature in the 2θ range 10°–100° with a step of 0.03°. The Scherrer equation was used to calculate the average crystallite diameter for selected nanopowders [30].

Density measurements were taken using the helium pycnometer (AccuPyc II 1340, FoamPyc V1.06, Micromeritics, USA). The measurements were taken in accordance with ISO 12154:2014 at temperature of 25 ± 2 °C.

Specific surface area (SSA) of nanopowders was determined using the surface analyser (Gemini 2360, V 2.01, Micromeritics, USA) by gas (nitrogen) adsorption method based on the linear form of the BET (Brunauer–Emmett–Teller) isotherm equation in accordance with ISO 9277:2010. Prior to performing measurements of density and specific surface area, the samples were subject to 2-h desorption in a desorption station (FlowPrep 060, Micromeritics, USA), at temperature of 220 °C with the flow of helium. Based on the determined specific surface area and pycnometric density, an average equivalent spherical particle diameter was determined. In this case, the assumption was that all particles are spherical and identical. The following equation was used for calculating the average particle size:

$$D = \frac{N \cdot 1000}{\text{SSA}_{BET} \cdot d} \tag{1}$$

where D—average size (diameter) of particles/nm, N—shape coefficient being 6 for the sphere, SSA$_{BET}$—specific surface area/m^2 g^{-1}, d—density/g cm^{-3}.

The zeta potentials (ζ) of samples were measured at 23 °C using laser Doppler electrophoresis analyser [Zetasizer Nano ZS (ZEN3600), Malvern Instruments Ltd]. Each sample powder (10 mg) was dispersed in 50 mL of deionised water (0.07 μS cm^{-1}, HLP 20UV, Hydrolab, Poland) by ultrasonication for 10 min in ultrasonic washer (30 W, Elma Schmidbauer GmbH, Germany). In order to obtain the isoelectric point (IEP), the pH of the suspension was

Table 1 SSA$_{BET}$, density (d), isoelectric point (IEP), particle size (D) values for ZrO$_2$–AlO(OH) nanopowders, as well as their mass loss (TG) and onset temperature (T_{on}) calculated from LT-DSC conducted in helium

| Composition	T_{on1}/ °C	Mass loss (up to 200 °C)/%	Mass loss (from 200 to 700 °C)/%	SSA$_{BET}$/ m^2 g^{-1}	d/ g cm^{-3}	Particle size (BET)/nm	IEP/ pH	T_{on2}/ °C
ZrO$_2$	10.8	2.85	2.49	114 [29]	5.17 [29]	10.2	6.02	–
ZrO$_2$–Al^{3+}/mass%								
2	15.1	3.28	2.81	145	5.25	8.1	6.06	–
5	12.0	7.30	3.80	214	4.79	6.0	6.81	–
8	12.4	9.11	5.01	276	4.49	5.0	6.83	–
10	7.5	3.37	2.46	138 [29]	5.08 [29]	8.5	6.66	–
12	10.7	25.8	2.88	326	4.34	4.4	6.36	–
ZrO$_2$–AlO(OH)/mass%								
30	6.7	3.00	4.54	146 [29]	4.58 [29]	10.2	5.73	474.0
40	7.3	3.05	4.83	128	4.47	10.5	7.30	465.5
50	4.9	3.57	7.35	152	3.76	10.5	7.44	413.7
56	7.1	3.55	7.27	123	3.62	13.0	7.12	430.1
60	9.3	2.83	7.82	124 [29]	3.94 [29]	12.3 [29]	7.01	440.7
67	7.3	3.12	8.63	128	3.53	13.0	7.24	420.0
80	8.1	1.37	10.85	119 [29]	3.49 [29]	14.5 [29]	7.91	441.7
90	–	8.47	23.00	78 [29]	3.23 [29]	23.7 [29]	8.48	288.2
96	7.1	1.25	14.06	124	2.84	17.0	8.51	403.2
99	7.7	5.87	14.81	170	2.69	13.0	9.10	391.6
AlO(OH)	9.5	2.20	15.50	173	2.99	11.6	9.51	383.5
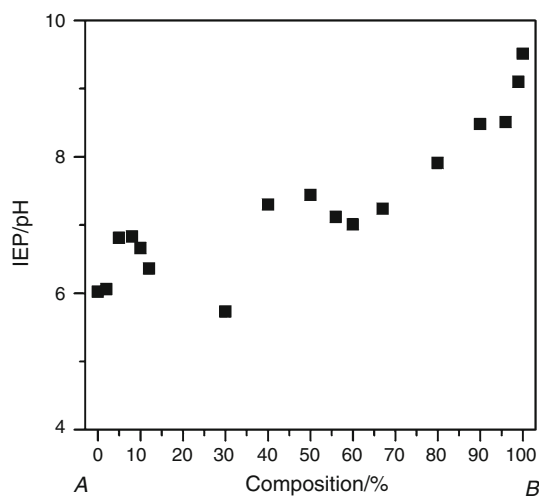
Fig. 4 Isoelectric point for ZrO$_2$ with different AlO(OH) content, where A = 100% ZrO$_2$ phase, B = 100% AlO(OH) phase

first adjusted to pH 11 by adding 0.2 M NaOH solution and changed several times to pH 2 by adding 0.2 M HCl solution using an automated titration system (titrator MPT-2, pH electrode type MV 114-S.C. SEN 0106, Malvern Instruments Ltd; vacuum degasser, P/N 0001-6353, Systec). The zeta potential of each sample was measured two times at every pH value, and the average zeta potential at a certain pH value was plotted against the pH value. The pH value where the zeta potential was zero was taken as the IEP.

Results and discussion

Figure 1 shows XRD diffraction patterns for chosen ZrO$_2$–AlO(OH) compositions. The XRD patterns for different compositions are presented before [29]. Here we show only some results in order to demonstrate how the phase composition changes with increasing amount of AlO(OH). Powders which contained 99 and 100% of AlO(OH) are characterised by pure boehmite [χ-AlO(OH) (JCPD 21-1307)] structure. ZrO$_2$ nanopowder without Al^{3+} addition is a mixture of tetragonal (JCPD 17-0293) and monoclinic zirconia (JCPD 86-1449). Samples containing
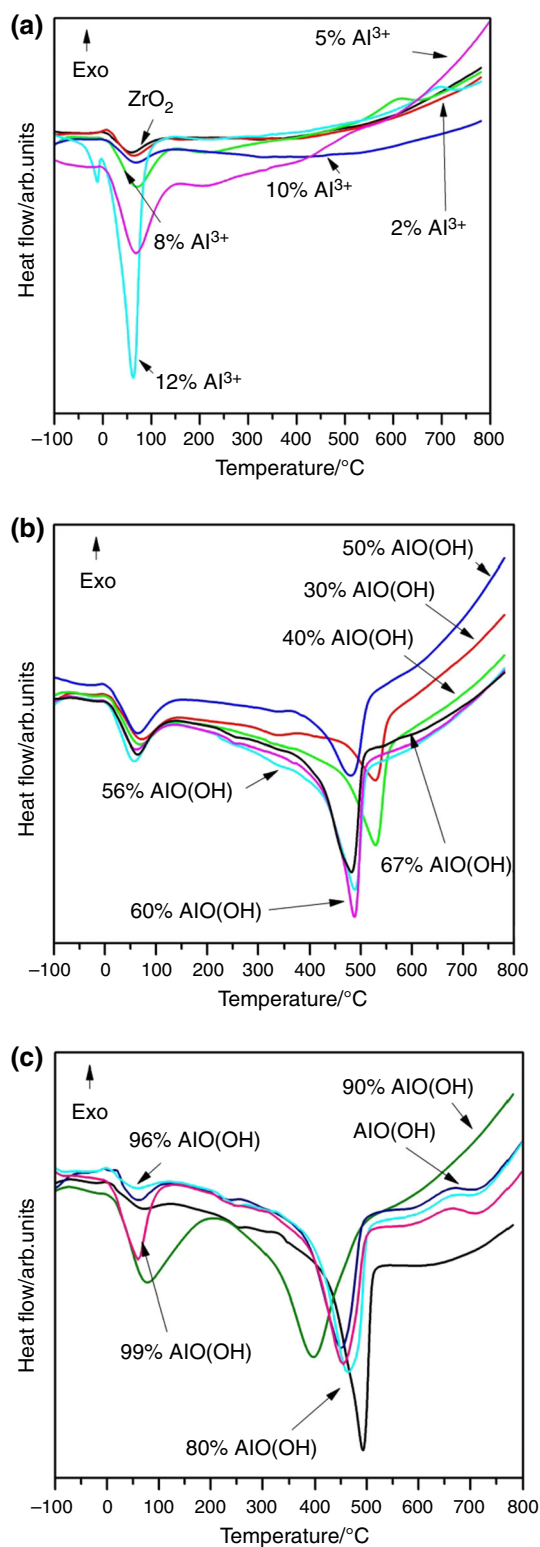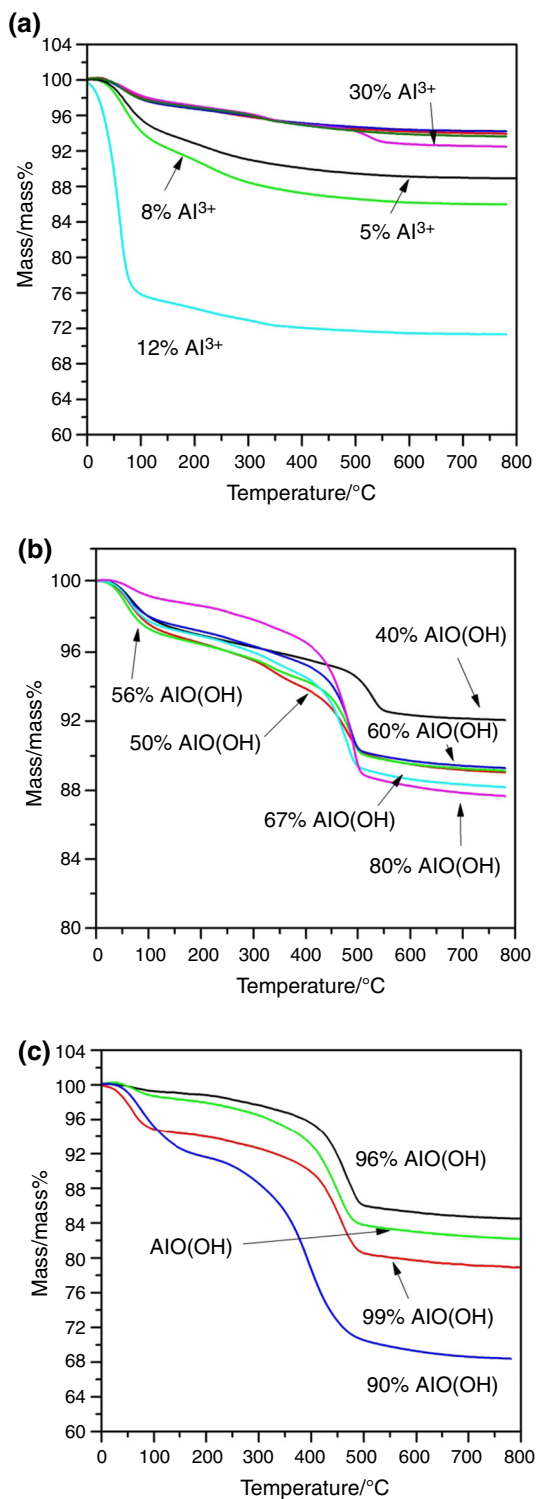
Fig. 5 LT-DSC curves for ZrO_2 with different AlO(OH) content, where **a** shows 100% ZrO_2, and ZrO_2 with 2–12% of Al^{3+} addition, **b** ZrO_2 with 30–67% of AlO(OH) additive and **c** represents 100% AlO(OH), and ZrO_2 with 80–99% of AlO(OH) additive
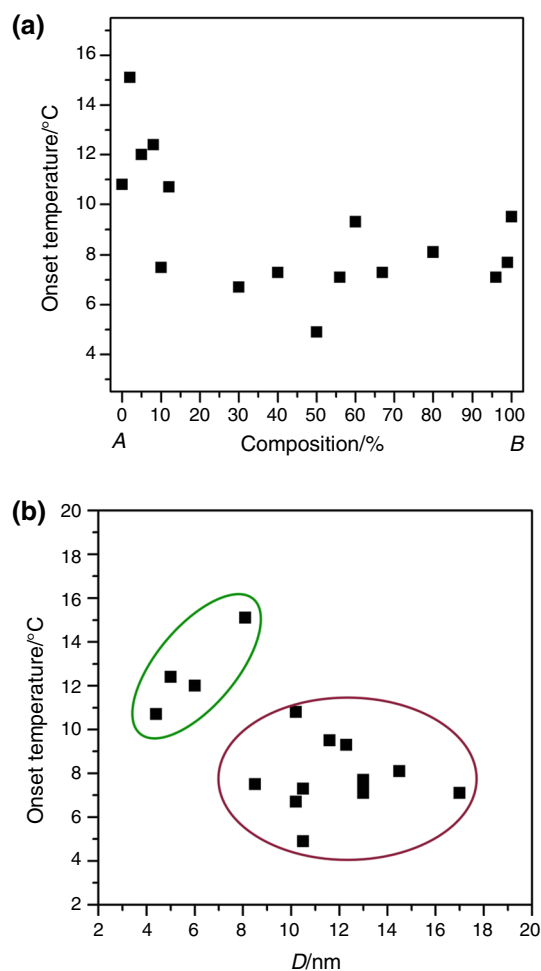

Fig. 6 Onset temperature (T_{on1}) dependence on the composition (**a**), and the onset temperature (T_{on1}) as a function of SSA_{BET}, where $A = 100\%$ ZrO_2 phase, $B = 100\%$ AlO(OH) phase

between 5 and 15% of Al^{3+} addition show diffraction patterns for only t-ZrO_2. Higher amount of AlO(OH) (between 30 and 90%) besides t-ZrO_2 phase also contains boehmite phase.

Our previous results [29] confirmed that boehmite phase appears in as-synthesised ZrO_2 samples from 30% of AlO(OH) additive. Below this value (up to 25% of Al^{3+}), ZrO_2–Al^{3+} creates solid solution (Al^{3+} doped ZrO_2) [29]. The temperature of microwave synthesis conducted by us was in the range from 258 to 263 °C, which was not high enough to obtain Al_2O_3 phase. α-Al_2O_3 is formed in a reactor with minimum crystallisation temperatures of 380 °C or higher [31]. In this work, microwave synthesis conditions ($T = 80$–270 °C) could only form χ-AlO(OH) [32] phase. However, according to hydrothermal Al_2O_3–H_2O phase diagram in the temperature range 310–380 °C, and after applying pressure higher than 17 MPa, α-AlO(OH) [31] is formed. It was mentioned above that

Fig. 7 TG curves for ZrO_2 with different AlO(OH) content, where **a** shows 100% ZrO_2, and ZrO_2 with 2–30% of Al^{3+} (pink colour—2%, blue colour—10%), **b** ZrO_2 with 40–80% of AlO(OH) additive, and **c** represents AlO(OH) and samples of ZrO_2 with 90–99% of AlO(OH) additive
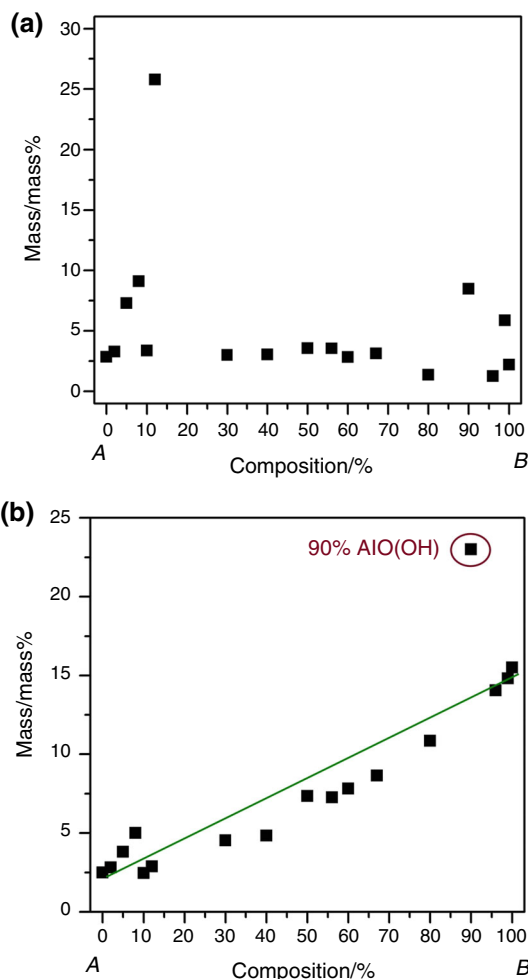

Fig. 8 Mass loss for the first transition for ZrO_2 with different AlO(OH) content (**a**), and for the second transition (**b**). Where $A = 100\%$ ZrO_2 phase, $B = 100\%$ AlO(OH) phase

boehmite phase transforms into Al_2O_3 after annealing in at least 800 °C, which was shown in [29] and [33].

Figure 2 shows SEM images for selected compositions in order to demonstrate the change of powders' morphology. It can be seen that all samples are rather uniform. With the higher content of AlO(OH) particles became more elongated. This fact is due to presence of Boehmite which is characterised by plate-like, elongated morphology [34].

Figure 3a shows SSA_{BET} results for all synthesised nanopowders. The spread of the values is from approximately 80 up to 326 m^2 g^{-1}. However, the biggest differences are observed for ZrO_2 with 12% Al^{3+} and 90% of χ-AlO(OH) (Table 1). Higher SSA_{BET} from 90% of AlO(OH) is due to apparent non-sphericity of particles as shown in Fig. 2. The increase in the specific surface area for the ZrO_2 and ZrO_2 with 2–12% of Al^{3+} is due to
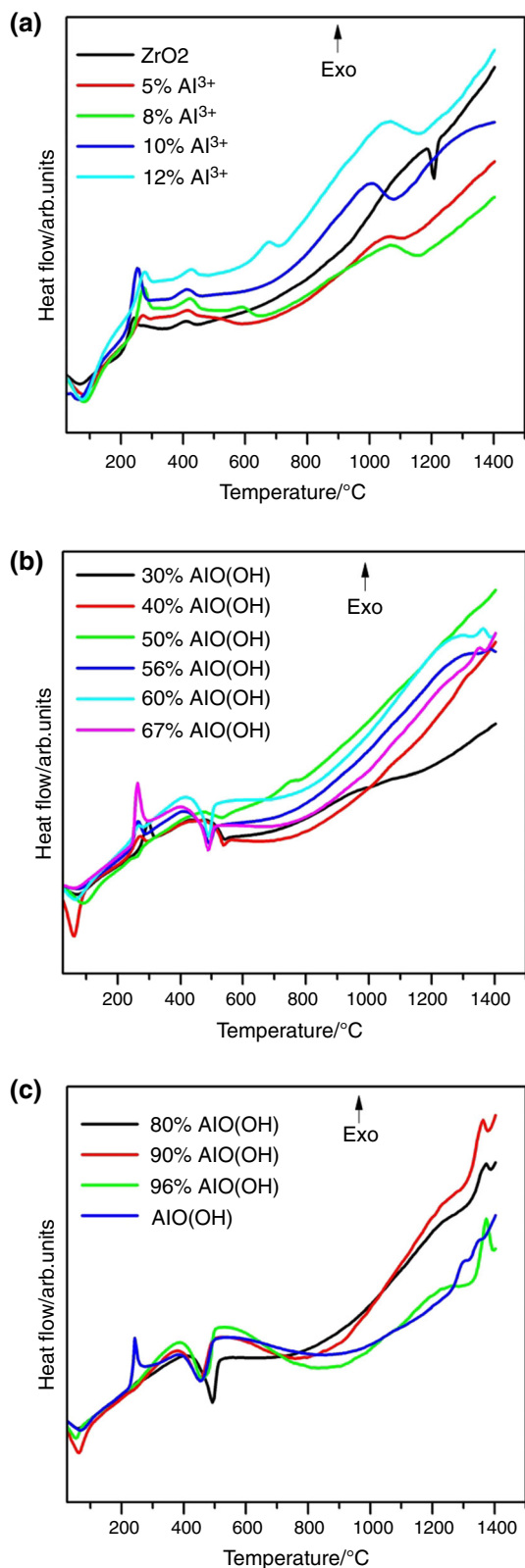
Fig. 9 HT-DSC curves for ZrO_2 with different AlO(OH) content, where **a** shows 100% ZrO_2, and ZrO_2 with 5–12% of Al^{3+}, **b** ZrO_2 with 30–67% of AlO(OH) additive, and **c** represents AlO(OH), and ZrO_2 with 80–96% of AlO(OH) additive

increasing amount of aluminium ions. Stable t-ZrO_2 is leading to the formation of smaller particles [35]. For the compositions ranging from 30 to 67% of AlO(OH), SSA_{BET} values are relatively constant declining slowly from 30 to 67% of AlO(OH). The SSA_{BET} decline could be attributed to an increased amount of non-outgassed water in the χ-AlO(OH) which remains in the system during the BET outgassing procedures. We think that it results in a small reduction in apparent surface of the sample as –OH groups occupy some available sites. Change in SSA_{BET} is also visible when shape of the particles changes]with the composition of ZrO_2 from 80% AlO(OH) to the pure AlO(OH)].

As it was described above, the SSA_{BET} values show 3 different regions approximately 0–12% Al^{3+}, 30–67 and 80–100% of AlO(OH) addition. Based on the combined measurements of SSA_{BET} and density (1) it was possible to report the variation of mean equivalent sphere size of particles in the nanopowder for all compositions investigated (Fig. 3b) [36]. It should be noted that particle density was found to monotonically decrease with % AlO(OH) in the system (Fig. 3c). This is as expected from the compound composition. It is possible to distinguish nanopowders with 3 different particle size ranges: form 4 to 8.5 nm, from 10 to 13 nm and from 13 up to 23 nm (Fig. 3b). The particle size increases, while the amount of Al^{3+} in the composition increases. Interestingly, for 0–12% compositions the SSA_{BET} increased sharply due to the rapid decrease in particle equivalent diameter. From 30 to 67% of AlO(OH), particle size increases slowly. However, for particles of 80% or higher the SSA_{BET} increases rapidly leading to a steep decrease in the equivalent particle diameter. From the SEM images of these samples (Fig. 2e, f), it is evident that the particle shape is not spherical. Particle aspect ratio or the non-sphericity increases with increasing AlO(OH) content for this composition range (from 80 to 100%). In order to test the assumption of particle size evaluation using SSA_{BET}, another method (Scherrer method) was used [30, 36]. The particle size range for selected compositions was following: 80% of AlO(OH): 18–25 nm, 90% of AlO(OH): 17–33 nm, 96% of AlO(OH): 9–17 nm, 99% of AlO(OH): 7–13 nm, and AlO(OH): 6–12 nm. Obtained results from Scherrer equations are in agreement with particle size calculated using Eq. (1).

Variation of density with composition is shown in Fig. 3c. The theoretical density of m-ZrO_2 and χ-AlO(OH) is 5.68 g cm^{-3} [37, 38] and 3.01 g cm^{-3} [31, 38], respectively. Pycnometric density of nano-ZrO_2, measured as a reference sample, is 5.17 g cm^{-3}. The difference between literature value, and that obtained in our examination maybe due to nanosized particles. At the same time, that difference could be caused by surface defects and

Table 2 Onset temperatures (T_{on}) for ZrO$_2$–AlO(OH) nanopowders calculated from HT-DSC conducted in air

| Composition	T_{on2}/°C	T_{on3}/°C	T_{on4}/°C	Comment
ZrO$_2$–Al^{3+}/mass%				
ZrO$_2$	242.6	–	1192.5	Phase composition: m + t-ZrO$_2$
5	230.0	–	1041.0	Particle size: 4–8.5 nm
8	240.0	595.1	1069.1	Water is released in T_{on1} and T_{on2} regions mainly
10	222.5	–	1001.7	
12	240.9	674.0	1052.0	
ZrO$_2$–AlO(OH)/mass%				
30	269.3	504.3	–	Phase composition: AlO(OH), m + t-ZrO$_2$
40	289.9	510.7	–	Particle size: 10–13 nm
50	274.1	477.8	–	Water is released in T_{on1}, T_{on2} and T_{on3} regions
56	244.6	443.6	1310.3w	
60	274.1	449.8	1321.5	
67	250.7	451.1	1349.3	
ZrO$_2$–AlO(OH)/mass%				
80	–	445.1	1330.9	Phase composition: AlO(OH), m + t-ZrO$_2$
90	–	387.4	1322.2	Particle size: 13–23 nm
96	–	402.8	1339.2	Water is released in T_{on1} and T_{on3} regions mainly
AlO(OH)	234.8	399.2	1267.2	

hydroxides [37]. The density value of χ-AlO(OH) is very close to the literature (Table 1; Fig. 3c). As it could have been predicted, values decrease when Al content in synthesised powder increases.

The isoelectric point (IEP) for ZrO$_2$ is 6.0 (Table 1; Fig. 4), which is in agreement with previously reported works [28, 39]. The IEP value for χ-AlO(OH) is 9.5 and is slightly higher than reported in the literature (9.1–9.2 [27, 40]). The difference may be caused by specific features of nanomaterials obtained by MHS. In case of ZrO$_2$ and χ-AlO(OH), the positive charge on the surface exists for pH < pH$_{(IEP)}$ while the negative charge appears in pH > pH$_{(IEP)}$ range. The increase of Al^{3+} content in ZrO$_2$ causes an increase in IEP values. This result is due to changes in nanopowder composition.

Figure 5 presents results of low-temperature DSC (conducted from − 100 up to 800 °C) for all synthesised nanopowders. We chose such a low starting temperature in order to observe clearly the onset temperature of released water. It is known that for this type of system the first endothermic transition is located at approximately 100 °C which corresponds to the evaporation of the physically adsorbed water [39]. The second one, between 200 and 500 °C, takes place due to the loss of chemically bonded water (hydroxides transformation) together with carbon dioxide [29, 39]. It can be seen that nano-ZrO$_2$ and ZrO$_2$ with AlO(OH) content below ∼ 30% are characterised by only one endothermic transition due to releasing of physically absorbed water (Fig. 5a). There is no signal from

chemically bonded water. The reason for such behaviour is the increasing amount of χ-AlO(OH) in the ZrO$_2$–AlO(OH) [27]. These findings are in agreement with results described above. It should be noted that such behaviour is very sensitive to composition. We found that the limit for the presence of chemically bonded water for ZrO$_2$–AlO(OH) materials investigated in helium is between approximately 12 and 30% of AlO(OH). Above 30% both physically bound and chemically bonded water is present. The type of released gasses during ZrO$_2$–AlO(OH) thermal treatment will be discussed further.

Obtained onset temperature (T_{on}) from DSC experiment for ZrO$_2$–AlO(OH) nanopowders is shown in Fig. 6 and Table 1. Figure 6a presents change in the onset temperature for the first endothermic event as a function of composition. Taking into account that estimation of starting point of the transition (T_{on1}) is quite difficult, we use the same approach and software (Proteus, Netzsch) in order to extract these values. Analysis of Fig. 6a shows that onset temperature for the evaporation of the physically adsorbed water differs for samples with lower content of Al. One possible explanation of such behaviour might be a reduced particle size. Figure 6b confirms a dependence of T_{on1} on the particle size. The smaller the average particle size, the higher the T_{on1}. Therefore, we would expect to obtain the lowest onset temperature for the powders with the smallest particle size and the highest specific surface area, especially while we are referring to the physically adsorbed water.
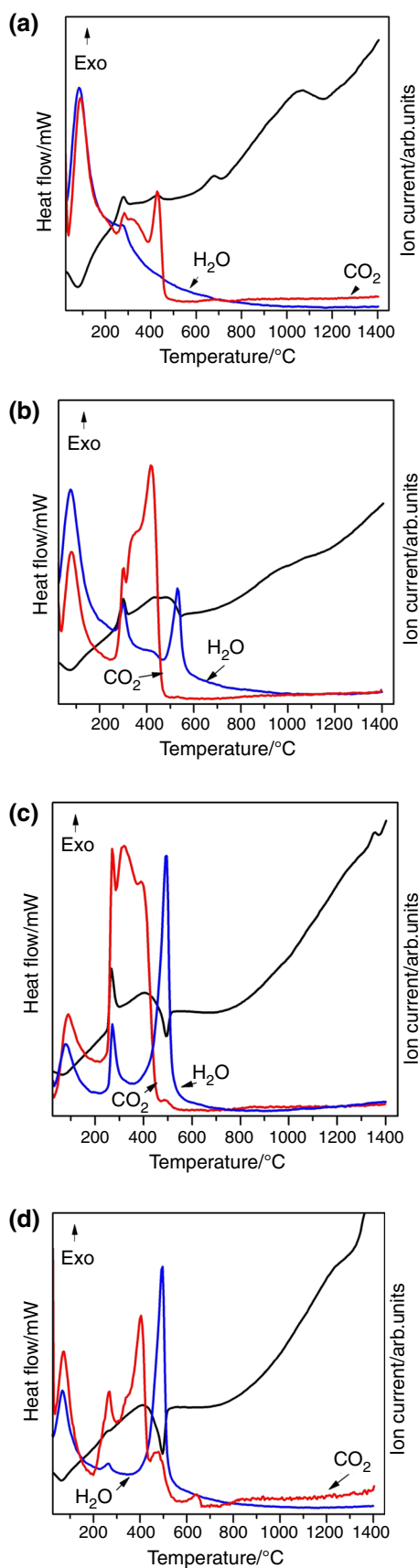
Fig. 10 HT-DSC–MS curves for ZrO_2 with different Al^{3+} or AlO(OH) content: **a** 12%, **b** 30%, **c** 67% and **d** 80%

On the other hand, T_{on2} for chemically bonded water shows rather linear dependence on composition (Table 1). The higher amount of AlO(OH), the lower onset temperature, which is most likely due to slower kinetics. There is clear exception for ZrO_2 nanopowder with 90% of AlO(OH) additive. Analysis of data collected in Table 1 shows such a high onset temperature for chemically bonded water desorption may be due to particle size and SSA_{BET}. The ZrO_2–90%-AlO(OH) sample is characterised by very small $SSA_{BET} \sim 78$ m^2 g^{-1} (compared to other samples) and relatively big particles size (~ 24 nm). These values differ from compositions by nearly 200%. Grabis et al. [3] have characterised ZrO_2–Al_2O_3 nanopowders produced by plasma techniques. They synthesised materials with very small SSA_{BET} (29–46 m^2 g^{-1}) which increased with alumina content. Authors suggest that the described behaviour is coupled with the reduction in m-ZrO_2 present.

Figure 7 shows sample mass loss (TG) during thermal treatment which is attributed to water and carbon dioxide release as we discussed above. In addition, Fig. 8 shows correlations between compositions and sample mass losses during the first (Fig. 8a) and second event (Fig. 8b). The desorption of physically absorbed water is the highest for the compositions at the ends of composition range [up to approximately 12% of Al^{3+} and AlO(OH)-10% ZrO_2]. Sample mass loss during second transition increases, while the content of AlO(OH) in the composition increases (Fig. 8b). This fact confirms our previous findings [29].

The high-temperature DSC was prepared in air in order to analyse thermal stability in broader temperature range (Fig. 9). Experiment curves were split into 3 figures: Fig. 9a: ZrO_2 with 5–12% Al^{3+}, Fig. 9b: ZrO_2 with 30–67% of AlO(OH) and Fig. 9c: ZrO_2 with 80–96% of AlO(OH). In this way, it is highlighted how particle size and materials' chemical composition change thermal characteristic of ZrO_2–AlO(OH). The onset temperatures for event 2, 3 and 4 are listed in Table 2. Transitions from RT up to approximately 450 °C are associated with the H_2O and CO_2 release (Fig. 10) [1, 41, 42], while the following endothermic transition is due to χ-AlO(OH) transformation and water release [33]. The forth, weak endothermic event above 1000 °C is related to particle growth and/or further ($t \rightarrow m$) ZrO_2 phase transformation [29].

Conclusions

The interdependence of composition, particle size, specific surface and thermal properties due to water adsorption has been demonstrated on an industrially relevant nanomaterial.

We showed how density, particle size and SSA$_{BET}$ values are changing for ZrO$_2$–AlO(OH) nanomaterials synthesised by MHS method in the whole range of compositions. The chosen synthesis method allowed to create crystalline ZrO$_2$–AlO(OH) nanopowders in simple and repeatable way. Obtained results, especially investigation of thermal behaviour, allow to establish suitable conditions for densification and sintering process of ZrO$_2$–AlO(OH) nanopowders.

Our research showed that nano-ZrO$_2$ and nano-ZrO$_2$ with 2–12% of Al^{3+} are characterised by only one endothermic transition due to releasing of physically adsorbed water (T_{on1}). There is no signal from chemically bonded water. The onset temperature for the evaporation of the physically adsorbed water was found to be relatively low and varied between the samples with lower content of AlO(OH). We found that T_{on1} depends on the particle size and boehmite presence. The smaller the particle size, the higher the T_{on1}. Specific surface area SSA$_{BET}$ has a direct influence on T_{on1}. The composition limit for the presence of only chemically bonded water was found to be between approximately 12 and 30% of Al^{3+}. Above 30% of AlO(OH) both physically bound and chemically bonded water is present. Experimental results show that ZrO$_2$–AlO(OH) nanopowders properties change above 30% of AlO(OH). For the composition below this value, Al^{3+} exists in solid solution (Al^{3+} doped ZrO$_2$).

Presented results allow to distinguish 3 groups of ZrO$_2$–AlO(OH) nanopowders, with distinct properties and thermal behaviour. The first group (I) of materials is ZrO$_2$ with Al^{3+} content up to 12% characterised by very small particles size ($\sim$ 4–10 nm), relatively high T_{on1}, and a visible endothermic transition at approximately 1050 °C. As-synthesised powders from group (I) indicate m + t-ZrO$_2$ phase composition. DSC–MS of these nanopowders conducted in air shows that water is release in T_{on1} and T_{on2} regions.

The second group (II) of materials is placed in the 30–67% range of AlO(OH) additive. This group is characterised by particles size in the range 10–13 nm, lower than (I) group value of T_{on1}, and lack of or shift of T_{on4} to the $\sim$ 1320 °C. As-synthesised powders of group (II) show AlO(OH) and m + t-ZrO$_2$ phases. DSC–MS of these nanopowders conducted in air is characterised by water release in T_{on1}, T_{on2} and T_{on3} regions.

The third group (III) of ZrO$_2$–AlO(OH) materials contains from 80 to 99% of AlO(OH). This group is characterised by larger particles size up to 23 nm, lower than (I) group value of T_{on1}, and shift of T_{on4} to the $\sim$ 1320 °C. As-synthesised powders of group (III) show AlO(OH) and m + t-ZrO$_2$ phases. DSC–MS of these nanopowders conducted in air is characterised by water release in T_{on1} and T_{on3} regions.

References

1. Zygmuntowicz J, Wiecinska P, Miazga A, Konopka K, Szafran M, Kaszuwara W. Thermoanalytical studies of the ceramic–metal composites obtained by gel-centrifugal casting. J Therm Anal Calorim. 2017. https://doi.org/10.1007/s10973-017-6647-z.
2. Mozafari RM. Nanomaterials and nanosystems for biomedical applications. 1st ed. Berlin: Springer; 2007. ISBN 978-1-4020-6289-6.
3. Grabis J, Rasmane D, Krumina A, Berzins M. Preparation and characterization of ZrO$_2$–Al$_2$O$_3$ particulate nanocomposites produced by plasma technique. In: Proceedings of the Estonian Academy of Sciences, Engineering, Dec 2006.
4. Bacic I, Mandic V, Curkovic L, Otmacic-Curkovic H, Kurajica S. Thermal and structural studies of sol–gel-derived yttria-doped ZrO$_2$ nanoparticles. J Therm Anal Calorim. 2017. https://doi.org/10.1007/s10973-016-5904-x.
5. Sakuma T, Hidehiro Y. High temperature grain boundary plasticity in ceramics. Mater Trans. 2009;50(2):229–35.
6. Yoshida H, Matsui K, Ikuhara Y. Low-temperature superplasticity in nanocrystalline tetragonal zirconia polycrystal (TZP). J Am Ceram Soc. 2012;5:1701–8.
7. Hulbert DM, Jiang D, Kuntz JD, Kodera Y, Mukherjee AK. Superplasticity of zirconia–alumina–spinel ceramic composite by spark plasma sintering of plasma sprayed powders. Scr Mater. 2007;56:1103–6.
8. Morita K, Hiraga K, Kim BN, Yoshida H, Sakka Y. Fabrication of nanocrystalline superplastic ZrO$_2$ ceramics. Mater Sci Forum. 2007;551:491–6.
9. Hana X, Lianga Z, Fenga L, Wanga W, Chena J, Xueb C, Zhaoa H. Co-precipitated synthesis of Al$_2$O$_3$–ZrO$_2$ composite ceramic nanopowders by precipitant and drying method regulation: a systematic study. Ceram Int. 2015;41:505–13.
10. Prasad K, Pinjari DV, Pandit AB, Mhaske ST. Synthesis of zirconium dioxide by ultrasound assisted precipitation: effect of calcination temperature. Ultrason Sonochem. 2011;18:1128–37.
11. Castillo JF, Isasi J, Perez M, Aldama I, Diaz-Guerra AP. Structural and cathodoluminescent properties of Zr$_{0.95}$Ce$_{0.05}$O$_2$ nanopowders prepared by sol–gel template methods. J Lumin. 2011;131:2128–32.
12. Ravichandran AT, Siriya Pushpa KC, Ravichandran K, Karthika K, Nagabhushana BM, Mantha S, Swaminathan K. Effect of Al doping on the structural and optical properties of ZrO$_2$ nanopowders synthesized using solution combustion method. Superlat Microstruct. 2014;75:533–42.
13. Vacandio F, Eyraud M, Knauth P, Djenizian T. Tunable electrical properties of self-organized zirconia nanotubes. Electrochem Commun. 2011;13:1060–2.

14. Yin W, Meng B, Meng X, Tan X. Highly asymmetric YSZ hollow fibre membranes. J Alloys Compd. 2009;476:566–70.

15. Benzaid R, Chevalier J, Saadaoui M. Fracture toughness, strength and slow crack growth in a ceria stabilized zirconia–alumina nanocomposite for medical applications. Biomaterials. 2008;29(27):3636–41.

16. Chandradass J, Kim MH, Bae DS. Influence of citric acid to aluminium nitrate molar ratio on the combustion synthesis of alumina–zirconia nanopowders. J Alloys Compd. 2009;470:L9–12.

17. Wei Z, Li H, Zhang X, Yan S, Lv Z, Chen Y, Gong M. Preparation and property investigation of CeO_2–ZrO_2–Al_2O_3 oxygen-storage compounds. J Alloys Compd. 2008;455:322–6.

18. Vecchio Ciprioti S, Bollino F, Tranquillo E, Catauro M. Synthesis, thermal behavior and physicochemical characterization of $ZrO2$/PEG inorganic/organic hybrid materials via sol–gel technique. J Therm Anal Calorim. 2017. https://doi.org/10.1007/s10973-017-6318-0.

19. Shukla S, Seal S, Vij R, Bandyopadhyay S. Effect of HPC and water concentration on the evolution of size, aggregation and crystallization of sol–gel nanozirconia. J Nanopart Res. 2002;4:553–9.

20. Lamas DG, Lascalea GE, Juarez RE, Djurado E, Perez L, Walsoe de Reca NE. Metastable forms of the tetragonal phase in compositionally homogeneous, nanocrystalline zirconia–ceria powders synthesised by gel-combustion. J Mater Chem. 2003;13:904–10.

21. Herrmann M, Seipel B, Schilm J, Nickel KG, Michael G, Krell A. Hydrothermal corrosion of zirconia-toughened alumina (ZTA) at 200 °C. J Eur Ceram Soc. 2005;25:1805–12.

22. Begand S, Oberbach T, Glien W. Corrosion behaviour of ATZ and ZTA ceramic. Bioceramics. 2007;19:1227–30.

23. Jin C, Gao L. Microstructure and mechanical performance of ZTA/$LaAl_{11}O_{18}$ composite prepared by a heterogeneous precipitation method. Mater Sci Eng. 2003;A360:275–9.

24. Chuang CC, Hsiang HI, Hwang JS, Wang TS. Synthesis and characterization of Al_2O_3–$Ce_{0.5}Zr_{0.5}O_2$ powders prepared by chemical coprecipitation method. J Alloys Compd. 2009;470:387–92.

25. Dudnik EV. Modern methods for hydrothermal synthesis of ZrO_2-based nanocrystalline powders. Powder Metall Met Ceram. 2009;48(3):238–48.

26. Szepesi CJ, Adair JH. High yield hydrothermal synthesis of nanoscale zirconia and YTZP. J Am Ceram Soc. 2011;12:4239–46.

27. Cinar S, Anderson DD, Akinc M. Influence of bound water layer on the viscosity of oxide nanopowder suspensions. J Eur Cer Soc. 2015;35:613–22.

28. Zych L, Haberko K. Zirconia nanopowder—its shaping and sintering. Solid State Phenom. 2003;94:157–64.

29. Malka I, Danelska A, Kimmel G. The influence of Al_2O_3 content on ZrO_2–Al_2O_3 nanocomposite formation—the comparison between sol-gel and microwave hydrothermal methods. Mater Today Proc. 2016;3:2713–24.

30. Patterson AL. The Scherrer formula for X-ray particle size determination. Phys Rev. 1939. https://doi.org/10.1103/PhysRev.56.978.

31. Suchanek WL. Hydrothermal synthesis of alpha alumina (α-Al_2O_3) powders: study of the processing variables and growth mechanisms. J Am Ceram Soc. 2010;93:399–412.

32. Suchanek W, Garce L. Alpha alumina supports for ethylene oxide catalysts and method of preparing thereof. U.S. patent application, Serial No. 11/750,188 (Sawyer Technical Materials, LLC, 2007).

33. Lamouri S, Hamidouche M, Bouaouadja N, Belhouchet H, Garnier V, Fantozzi Trelkat JF. Control of the γ-alumina to α-alumina phase transformation for an optimized alumina densification. Bol Soc Esp Cerám Vidr G. 2016. https://doi.org/10.1016/j.bsecv.2016.10.001.

34. Liu S, Chen C, Liu Q, Zhuo Y, Yuan D, Dai Z, Bao J. Two-dimensional porous g-AlOOH and g-Al_2O_3 nanosheets: hydrothermal synthesis, formation mechanism and catalytic performance. RSC Adv. 2015. https://doi.org/10.1039/c5ra09772j.

35. Opalinska A, Malka I, Dzwolak W, Chudoba T, Presz A, Lojkowski W. Size-dependent density of zirconia nanoparticles. Beilstein J Nanotechnol. 2015;6:27–35.

36. Wejrzanowski T, Pielaszek R, Opalińska A, Matysiak H, Łojkowski W, Kurzydłowski KJ. Quantitative methods for nanopowders characterization. Appl Surf Sci. 2006;253:204–8.

37. Scheffler M, Colombo P. Cellular ceramics: structure, manufacturing, properties and applications. New York: Wiley; 2005. ISBN 978-3-527-31320-4.

38. Viswabaskaran V, Gnanam FD, Balasubramanian M. Effect of MgO, Y_2O_3 and boehmite additives on the sintering behaviour of mullite formed from kaolinite-reactive alumina. J Mater Process Technol. 2003;142:275–81.

39. Zhou M, Xu L, Xi X, Li P, Dai W, Zhu W, Shui A, Zeng L. Investigation on the preparation and properties of monodispersed Al_2O_3-ZrO_2 nanopowder via co-precipitation method. J Alloys Compd. 2016;678:337–42.

40. Gallios G, Matis P, Kostas A. Mineral processing and the environment. Berlin: Springer; 1998. ISBN 978-94-017-2284-1.

41. Madej D. Hydration, carbonation and thermal stability of hydrates in $Ca_{7-x}Sr_xZrAl_6O_{18}$ cement. J Therm Anal Calorim. 2017. https://doi.org/10.1007/s10973-017-6726-1.

42. AugustoT Restivo G, Durazzo M, HomemdeMello-Castanho SR, CuglerMoreira A, Graciano S, BridiTelles V, SoaresTenorio JA. Low-temperature densification of ceramics and cermets by the intermediary stage activated sintering method. J Therm Anal Calorim. 2017. https://doi.org/10.1007/s10973-017-6560-5.